Mon. Not. R. Astron. Soc. **374,** 1056–1066 (2007) doi:10.1111/j.1365-2966.2006.11221.x

The cluster of galaxies LCDCS-S001: basic spectroscopic data and stellar population

S. B. Rembold★ and M. G. Pastoriza

Instituto de Física, Universidade Federal do Rio Grande do Sul, Av. Bento Gonçalves 9500, CEP 91350-050, Porto Alegre, Rio Grande do Sul, Brazil

Accepted 2006 October 20. Received 2006 October 19; in original form 2006 August 31

ABSTRACT

We present kinematic parameters and stellar population properties of selected galaxies in the high-redshift ($z = 0.7$) galaxy cluster LCDCS-S001, determined by spectroscopic data obtained with the Gemini multi-object spectrograph instrument in the Gemini South Observatory. The objects were selected in an i'-band cluster field image, and multi-object spectroscopic observations centred at 7500 Å were performed for 40 objects. Spectral features were successfully identified for 20 objects, and used to determine the redshift of the cluster. We found that 12 objects are cluster members and estimate a median redshift of 0.709 for this cluster. The relative velocities of the cluster members were used to estimate the projected cluster mass, which was found to be $3.54 \times 10^{14+2.33}_{-1.41}$ $M_{\odot}$. Lick and $D_n(4000)$ indices were measured and used to determine the stellar population properties of the galaxies, by means of a spectral synthesis through Bruzual & Charlot evolutive models. We found that the bulk of stellar population for the cluster members has a spectrum compatible with solar metallicity and an age between 3.0 and 7.0 Gyr; with only one exception, the flux contribution of younger ($t \leqslant 1.0$ Gyr) stars in the spectra does not exceed 25 per cent at 4200 Å. Emission [O II] lines were detected for four galaxies, all of which showing a stronger contribution of young stars compared with other cluster galaxies. The equivalent width of the [O II]λ3727 emission line was compared with Magris, Binette & Bruzual models for H II regions. We found good correspondence between our values and the theoretical predictions for solar metallicity and with star formation time-scales $1.0 < \tau < 3.0$ Gyr.

Key words: galaxies: clusters: general – galaxies: clusters: individual: LCDCS-S001 – galaxies: high-redshift – galaxies: stellar content.

1 INTRODUCTION

It is well known that clusters of galaxies are formed by three components: dark matter, intracluster medium (ICM) and galaxies. These components are affected by different physical processes evolving differently one from the other. Although these components may interact with each other this mechanism is still an open question.

Besides, clusters of galaxies are never isolated, being far from closed systems and may be affected by near large-scale structures. Consequently, the cluster parameters evolve in different time-scales depending on thermal, dissipative and dynamical properties of its mass component (Postman, Lubin & Oke 1998). The cluster mass controls the main properties of the system and its environment.

There are many observational facts that show strong difference between cluster galaxies at different redshifts. For example, there is evidence that a significant fraction of early-type galaxies in MS 1054-03 ($z = 0.83$) are merging, and that results in a significant scatter in the colour–magnitude relation relative to what is observed at $z < 0.5$ (van Dokkum et al. 2000). The fraction of cluster galaxies which show star formation is significantly higher at $z = 0.75$ (∼50 per cent) than the fraction of the current epoch or even at $z = 0.5$ (Postman et al. 1998). It is quite important, therefore, to perform spectroscopic and photometric observations of cluster galaxies at redshift $0.5 < z < 1.0$, in order to understand how the cluster environment affects the galaxy evolution.

In this paper, we present the kinematic of the galaxy cluster candidate LCDCS-S001, selected from the Las Campanas Distant Cluster Survey (Gonzalez et al. 2001), with an estimated redshift of $z \sim 0.47$, as well as the stellar population properties of the cluster members. This paper is structured as follows. In Section 2 we present the observation and data reduction; in Section 3 we show the redshift determination for the galaxies and the determination of the median cluster redshift; in Section 4 we present the projected mass determination for the cluster; in Section 5 we detail the line indices measurements for absorption and emission lines, the spectral synthesis and the results regarding the stellar population parameters obtained for the cluster members; in Section 6 we present the determination

★E-mail: sandro.rembold@ufrgs.br

of the absolute magnitudes and luminous masses estimations for the galaxies; our conclusions are drawn in Section 7. Throughout the paper, we will use $H_0 = 71$, $\Omega_M = 0.27$ and $\Omega_V = 0.73$.

2 OBSERVATIONS AND DATA REDUCTION

The spectroscopic observations were conducted using the Gemini multi-object spectrograph (GMOS) of the Gemini South observatory. The GMOS mask was built using as reference an i' filter image obtained with GMOS, which covered an area of 330×330 arcsec^2, with a total integration time of 300 s, using spatial binning of 2×2 pixels, with spatial scale of 0.146 arcsec pix^{-1}. Objects of interest were chosen based on their magnitude, apparent morphology and relative projected distance. Complete photometric data of all galaxies in the observed field will be given in a forthcoming paper. Two masks were needed to include 40 objects. Each mask was exposed 1200 s in order to reach a signal-to-noise ratio (S/N) higher than 3 per angstrom for objects of magnitude $i' = 20$.

The first steps were done using the standard GMOS reduction packages of IRAF. The raw two-dimensional multi-object images were bias-subtracted and flat-fielded using calibration images obtained at the same telescope configuration. A wavelength calibration was achieved by use of CuAr lamp images. The sky and the sources extraction is a very difficult task for objects with such low signal. First, the sky contribution is very hard to determine accurately for two-dimensional spectra with small spatial coverage; secondly, a one-dimensional spectrum of faint objects are hard to correctly, trace and extract. The GMOS reduction packages estimates the sky contribution in a two-dimensional spectrum by fitting a function to the pixel points at each column of the slit (spatial dimension) in regions around the source, defined previously by the user. For short slits, the non-parallelity of the spectral dimension of the slit with the lines in the CCD causes the contamination of the regions defined as having purely sky contribution in a specific wavelength. This causes a superestimation or a subestimation of the sky contribution and the introduction of false features in the extracted spectra. To trace low-S/N objects, the GMOS tasks fail to determine the centre of the brightness profile, even in cases where this detection is easily feasible by eye.

To deal with these two important problems, we have adopted the following approach. With the IRAF task APALL, we have made two extractions for each object, both centred in the apparent centre of the brightest profile of the object at a specific wavelength. The first extraction (f_1) was set to the apparent diameter of the source, and the second (f_2) to the full diameter of the slit. Due to the low S/N, a fraction of all sources could not be traced, therefore the extractions of their spectra was not useful; for the fraction of the slits which were correctly traced, we have identified the general behaviour of the tracing function. Fig. 1 shows the tracing function (a Legendre polynomial of order 2) of 17 sources which were correctly traced by the task APALL. It is obvious from this figure that there is a common mean function which fits all slits with good accuracy, variations are inside 0.25 pixels from the mean. We have then determined the mean Legendre coefficient for the tracing and re-extracted the sources for which the tracing was not successful using this coefficient as a fixed parameter.

Having these two extractions centred in the object but with different apertures, we determine the pure emission of the object using the following considerations. The extractions can be written as

$$f_1(x) = \mathrm{SKY}_{\text{Å}}(x)\,\Delta y_1 + \mathrm{OBJ}(x), \tag{1}$$

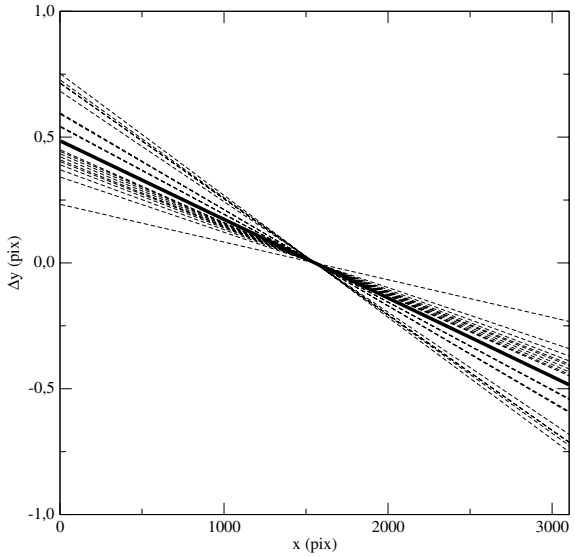

Figure 1. Tracing functions (pixel displacement Δy of the centre of the profile as a function of the x location in the CCD) of the sources in the mask # 1.

$$f_2(x) = \mathrm{SKY}_{\text{Å}}(x)\,\Delta y_2 + \mathrm{OBJ}(x), \tag{2}$$

where $\mathrm{SKY}_{\text{Å}}(x)$ is the mean sky contribution at the (spectral) pixel x per angstrom, Δy_1 and Δy_2 are the extraction widths and OBJ (x) is the integrated object contribution at the pixel x. Simple arithmetic leads us to

$$\mathrm{OBJ}(x) = \frac{\Delta y_1}{\Delta y_2 - \Delta y_1}\left[\frac{\Delta y_2}{\Delta y_1} f_1(x) - f_2(x)\right], \tag{3}$$

and the sky contribution is straightforward to determine. We still have to take into account the fact that, at the slit borders, there will be sky contribution losses due to the variations in the object centre, which causes the centre of the extraction to vary as a function of x. This is done by correcting the sky contribution by a multiplication factor equal to the ratio of the flux which is lost in the tracing.

After these procedures, the three partial spectra of each object were combined. This combination is also a crucial step of the data reduction. Calculating the median of the spectra is very useful in cases where there are many extractions, but for three extractions it basically chooses the intermediate value among each three, what produces a not very robust result; the use of the average provides better continuum determination but does not allow cosmic rays remotion. In order to minimize both problems, we have used the following prescription to combine the separate images: in a given wavelength, for each pair of the three measured values, the average and the s.d. σ of the mean was determined; if any value exceeded 3σ from the average, this value was discarded and the average of the other two was the result; if no value among the three satisfied in this condition, then the average of the three points was taken. This clipping algorithm has the advantages of the average calculation while allowing correction for deviant pixels.

The final step was to flux calibrate the spectra, which was done using a spectrophotometric standard star. The standard star spectrum did not cover the full wavelength range, being useful only up to 7000 Å. The IRAF task CALIBRATE was used to determine the flux calibration. No telluric correction was applied, once telluric standard stars were not observed.

Although we took a lot of care in the data reduction, the very intense sky emission lines still present features around 6000–11 000 Å

Table 1. Prominent features, i'_{AB} integrated magnitudes and redshifts of the observed galaxies.

ID	RA (2000) (h m s)	Dec. (2000) (° ′ ″)	i'_{AB}	z	Prominent features
120	10 06 25.20	−12 58 56.6	21.42	0.2201	CH λ4300, Hβ, [O III] λ4959, [O III] λ5007, Mg2, Mg I λ5170, [N II] λ5200, Hα, [S II] λ6730
146	10 06 21.10	−12 59 07.7	21.50	0.3910	H9, Ca II K, Ca II H, Hδ, CH λ4300, Hβ, Mg2, [N I] λ5200
157	10 06:18.37	−12 59 11.6	21.68	0.7074	H12, H9, H8, Ca II K, Ca II H, Hδ, CH λ4300, Hγ
175	10 06 16.17	−12 59 06.9	21.58	0.7064	H10, Ca II K, Ca II H, Hδ, CH λ4300
180	10 06 14.90	−12 59 07.9	21.75	0.6508	Ca II K, Ca II H, CH λ4300, Hγ
182	10 06 14.71	−12 59 50.1	21.17	0.7086	Ca II K, Ca II H, Hδ, CH λ4300, Hγ, Mg2
224	10 06 21.20	−12 57 35.5	21.90	0.7091	H12, H11, H10, H9, Ca II K, Ca II H, Hδ, CH λ4300
226	10 06 20.94	−12 57 42.5	21.47	0.6983	H10, H9, H8, Ca II K, Ca II H, Fe I λ4045, Hδ, CH λ4300, Fe I λ4383
236	10 06 19.70	−12 58 23.9	21.77	0.7173	H10, H8, Ca II K, Ca II H, Hδ
237	10 06 19.22	−12 58 17.0	20.82	0.2305	Hβ, [O III] λ5007, Mg2
241	10 06 18.69	−12 58 21.0	20.68	0.7090	H10, Ca II K, Ca II H, CH λ4300
244	10 06 18.45	−12 58 32.9	21.48	0.7093	H8, Ca II K, Ca II H, Hδ, CH λ4300, Hγ, [O III] λ5007
266	10 06 15.80	−12 58 28.8	21.89	0.7784	H10, H9, H8, Ca II K, Ca II H
273	10 06 13.51	−12 58 23.1	21.96	0.7055	Ca II K, Ca II H
302	10 06 24.77	−12 57 10.2	21.53	0.7090	H9, H8, Ca II K, Ca II H, Hδ, CH λ4300, Fe I λ4383, Hγ
308	10 06 22.14	−12 56 53.3	21.01	0.5550	Ca II K, Ca II H, Hδ, CH λ4300, Fe I λ4383, Hβ
318	10 06 19.46	−12 57 04.0	21.10	0.7077	H9, H8, Ca II K, Ca II H, Hδ, CH λ4300, Fe I λ4383, Hβ, Mg2
426	10 06 16.99	−12 56 24.9	20.87	0.6425	Ca II K, Ca II H, Hδ, CH λ4300, Hγ
428	10 06 17.14	−12 56 41.6	21.35	0.7784	Ca II K, Ca II H
1481	10 06 20.30	−12 58 36.7	21.08	0.7107	H10, Ca II K, Ca II H, CH λ4300

in some of the spectra. 30 of a total of 40 objects observed, had final, reduced spectra with good sky correction and S/N.

3 REDSHIFT DETERMINATION AND CLUSTER KINEMATICS

The most brightest absorption and emission lines observed in the spectra of the sample of galaxies were identified. The Doppler shift was measured separately for each line. In general, the Ca II K and H lines are the easiest to find; other notable features are the Balmer lines (especially Hδ) and G λ4300. We have successfully identified spectral features for 20 objects listed in Table 1.

The redshift of each galaxy was determined by the average recession velocity given by the individual lines. Cross-correlation methods with kinematic standard stars were not used due to the very long overheads involved in the GMOS observations of such templates. Redshifts were corrected for the observed radial velocity effects using the RVCORRECT task of IRAF. The last column of Table 1 gives this value for each galaxy. It is clear from this column that a large fraction of the objects lie in a very narrow range of redshifts around $z = 0.7$, what implies that a physical system including a large number of galaxies is present at this redshift. For the 20 objects for which it was possible to determine a spectroscopic redshift, 12 have redshifts between 0.69 and 0.72, being strongly concentrated at the median redshift of 0.709. Fig. 2 shows the full area imaged by GMOS (left-hand panel) and the galaxies selected for spectroscopy (right-hand panel). Fig. 3 shows the distribution of the confirmed objects (left-hand panel) and the optical centre of the cluster (right-hand panel). The i'-band images and contours of the confirmed member galaxies

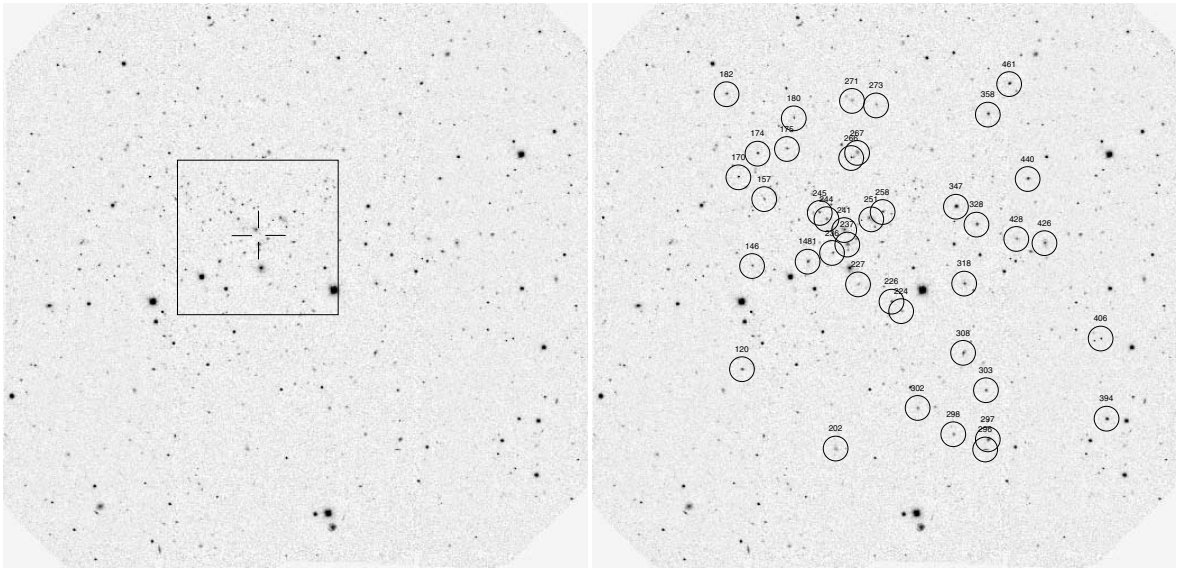

Figure 2. The full area imaged by GMOS (left-hand panel) and the objects selected for spectroscopy (right-hand panel).

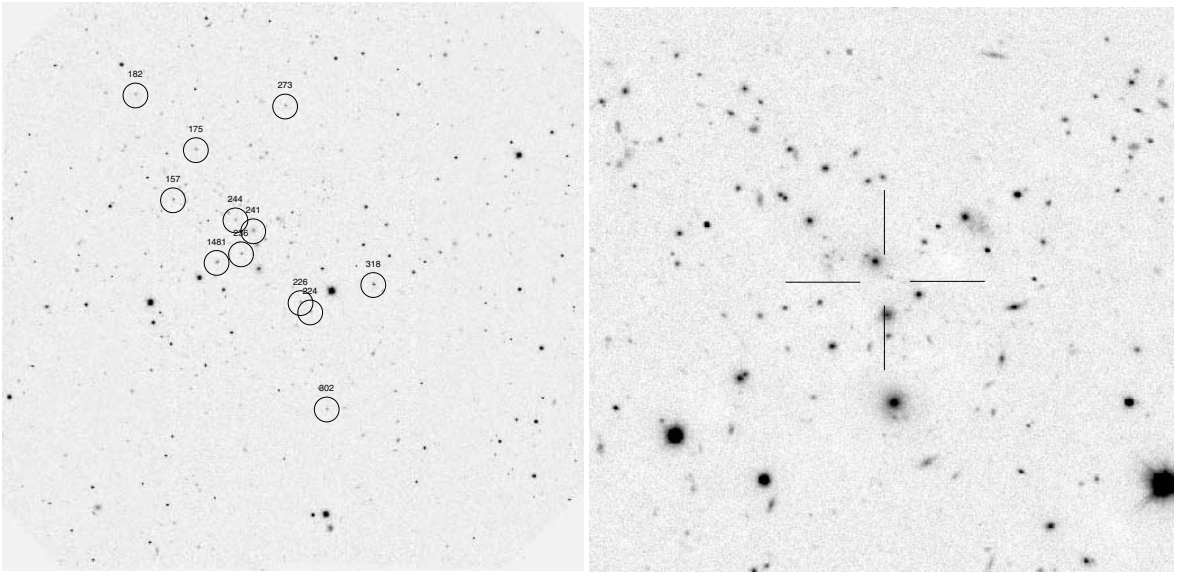

Figure 3. Projected distribution of the confirmed cluster members (left-hand panel) and the visual centre of the cluster (right-hand panel).

are presented in Fig. 4. Fig. 5 presents the relative velocity distribution of galaxies with respect to the median value. Relative velocities were calculated using $\Delta\, \upsilon = c(z - z_{\rm m})/(1 + z_{\rm m})$, where $z_{\rm m}$ is the median redshift. As this figure shows, the 12 galaxies have relative velocities well inside 3500 km s^{-1}, a value frequently used as a limit for cluster members (Postman et al. 1998). No obvious substructure is seen in this diagram; this could indicate that the system is not dynamically young, but a strong conclusion cannot be taken because of the low number of objects. We estimated the velocity dispersion from this distribution of velocity offsets and found $\sigma = 727 \pm 185$ km s^{-1}. In Fig. 6 we show the spectra of the confirmed cluster members, where we identify the most prominent lines.

4 MASS DETERMINATION

There are several methods of mass determination through optical kinematics, all of which are based upon the assumption of virialization. Even if there is strong evidence that a large fraction of cluster at $z \sim 1$ is dynamically young (Henry 2002), Small, Sargent & Hamilton (1998) have shown that mass estimators based on the virial theorem gives reasonable results, also when the considered system is not under virial equilibrium. We have calculated the projected mass $M_{\rm P}$ of the cluster, which is defined by

$$M_{\rm P} = \frac{10.2}{G \times (N - 1.5)} \sum_{i}^{N} (\Delta \upsilon_i)^2 R_{{\rm P},i}, \qquad (4)$$

where G is the gravitational constant, $\Delta\, \upsilon_i$ is the radial velocity offset of each galaxy relative to the average, N is the number of galaxies and $R_{{\rm P},i}$ is the (estimated) projected clustocentric distance of each galaxy (Postman et al. 1998). An estimate of the cluster centre was obtained by visual inspection of the distribution of the galaxies belonging to the cluster; as can be seen in the right-hand panel of Fig. 3, the number density of non-stellar objects has a remarkable peak around RA (2000) = $10^{\rm h}06^{\rm m}18\overset{\rm s}{.}9$, Dec. (2000) = $-12^\circ 58' 19\overset{''}{.}2$. This centre determination is reinforced by the presence of an intense radio emission at this position, as will be discussed in Section 6. The calculated projected clustocentric distances of the galaxies are given in column 20 of Table 2. Following the uncertainty estimates in $M_{\rm P}$ from Heisler, Tremaine & Bahcall (1985), the estimated the projected mass as $3.54 \times 10^{14}\ ^{+2.33}_{-1.41}$ M$_\odot$, corresponding to the mass of a rich cluster of galaxies and comparable to clusters of richness 1.

5 STELLAR POPULATION

High-redshift galaxies are an important source for information for the star formation history and chemical enrichment of the Universe. Nevertheless, extracting this information from such objects is a challenge even to modern telescopes because both multicolour photometry and spectroscopy, need good spatial and spectral resolution, as well as a long integration time.

A low number of derivations of galaxy ages and metallicities at intermediate and high redshifts have been obtained (see e.g. Barr et al. 2005; Demarco et al. 2005; Jorgensen et al. 2005). New data are important to confirm these previous results. In this work, we present a first approach for the star formation history of the 12 galaxies members of the cluster LCDCS-S001, which will help to understand the overall evolutive scenario of these systems. This was done by extracting equivalent widths (EWs) of both emission and absorption lines and by comparing these values with spectrophotometric models (Bruzual & Charlot 2003).

5.1 Lick indices

The rest-frame wavelength range 3500–5000 Å contains many important spectral absorption features. Besides the Balmer lines, several metallic lines (like Fe ıλ 4531) are present, as well as molecular bands like CN_1 and CN_2. The EWs of the brightest absorption lines were measured following the definition of the Lick system (Worthey & Ottaviani 1997; Trager et al. 1998), listed in Table 3. Prior to the measurements of EWs and pseudo-continua, the spectra were normalized to the flux at λ4200 Å.

Lick indices measurements for any galaxy must be corrected to line broadening due to its stellar velocity dispersion, which tends to increase the EW of a given line, especially the atomic ones (Longhetti el al. 1998). Our data were not corrected by velocity dispersion once our spectra at such high redshift have low S/N.

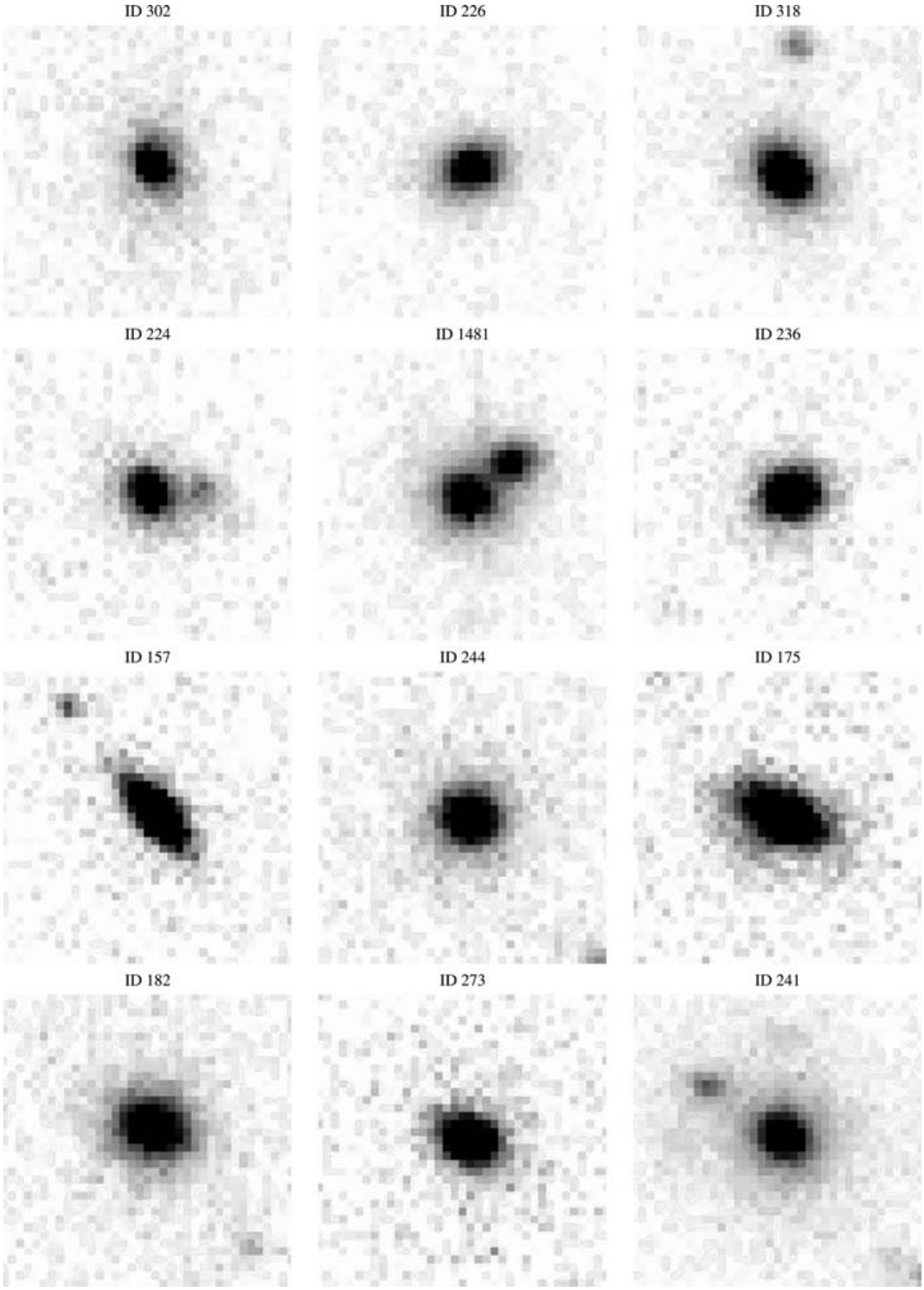

Figure 4. i'-band images and contours of the confirmed cluster galaxies (all frames are 5.33 × 5.33 arcsec^2).

We have measured 10 Lick indices and pseudo-continua of the objects, as well as the $D_n(4000)$ index, which reflect the properties of the underlying stellar population. The index measurements are presented in Table 2.

5.2 Stellar population synthesis

The measured indices and pseudo-continua were used to study the stellar population properties of the galaxies. Our main goal in this

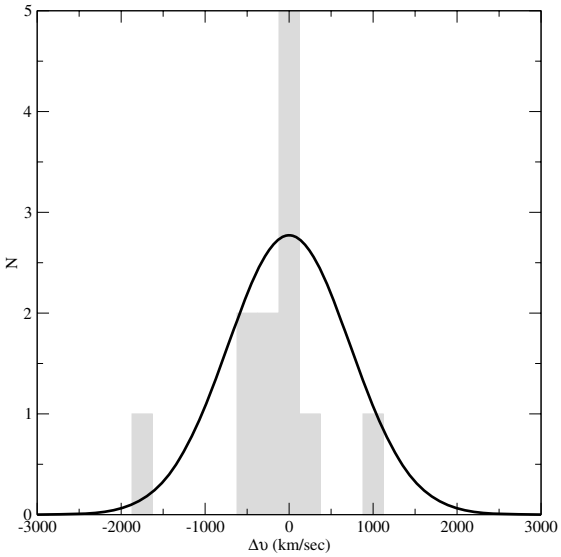

Figure 5. Distribution of redshifts around the median value. The estimated velocity dispersion is $727 \pm 185\,\mathrm{km\,s^{-1}}$.

section is to describe the age distribution of the stellar population in these galaxies. Due to the low S/N of the spectra and the limited number of observed absorption lines, we will limit this section to infer age distribution of the stellar populations and get some insights about their metallicity. There are several evolutionary models like Bruzual & Charlot (2003) and Maraston (2005). In this paper, we have used the Bruzual & Charlot (2003) evolutionary stellar population models; given the quality of our data, the use of more sophisticated models are expected to produce roughly the same results. This model is based on a high-resolution library of observed stellar spectra which makes it possible to derive a detailed spectral evolution of single stellar populations at a resolution of 3 Å between 3200 and 9500 Å, in a wide range of metallicities. There are many free parameters in these prescriptions, like the initial mass function (IMF), the attenuation by dust and the stellar evolution prescription. To limit the number of free variables in our analysis we fix the IMF as that of Salpeter (1955). Also, we used the *Padova 1994* tracks, as recommended by Bruzual & Charlot (2003).

For the chosen cosmological model ($H_0 = 71$, $\Omega_\mathrm{M} = 0.27$ and $\Omega_\mathrm{V} = 0.73$), the age of the Universe at a redshift $z = 0.7$ is around 7 Gyr; therefore, we have extracted a set of eight spectra from the Bruzual & Charlot (2003) models, with ages 0.1, 1.0, 3.0 and 7.0 Gyr and metallicities $Z = 0.02$ (solar) and $Z = 0.004$.

Since our index values are not corrected for velocity dispersion, we have convolved the spectra of the models with a velocity dispersion of $150\,\mathrm{km\,s^{-1}}$. Even this being a crude correction, which overestimates the synthetic indices for low-mass galaxies, we do not expect large errors, because the dependence of index values on velocity dispersion is not strong at this range.

The synthesis method that we have applied consists in obtaining for each observed spectrum the linear combination of a template (synthetic) spectra which minimizes the following relation:

$$2\chi = \sum_{i=1}^{N} \left| \frac{I_{\mathrm{TOT},i} - I_{\mathrm{MEA}_i}}{K_i} \right| + \sum_{i=1}^{N-1} \left| \frac{P_{\mathrm{TOT},i} - P_{\mathrm{MEA}_i}}{P_{\mathrm{MEA},i}} \right|, \qquad (5)$$

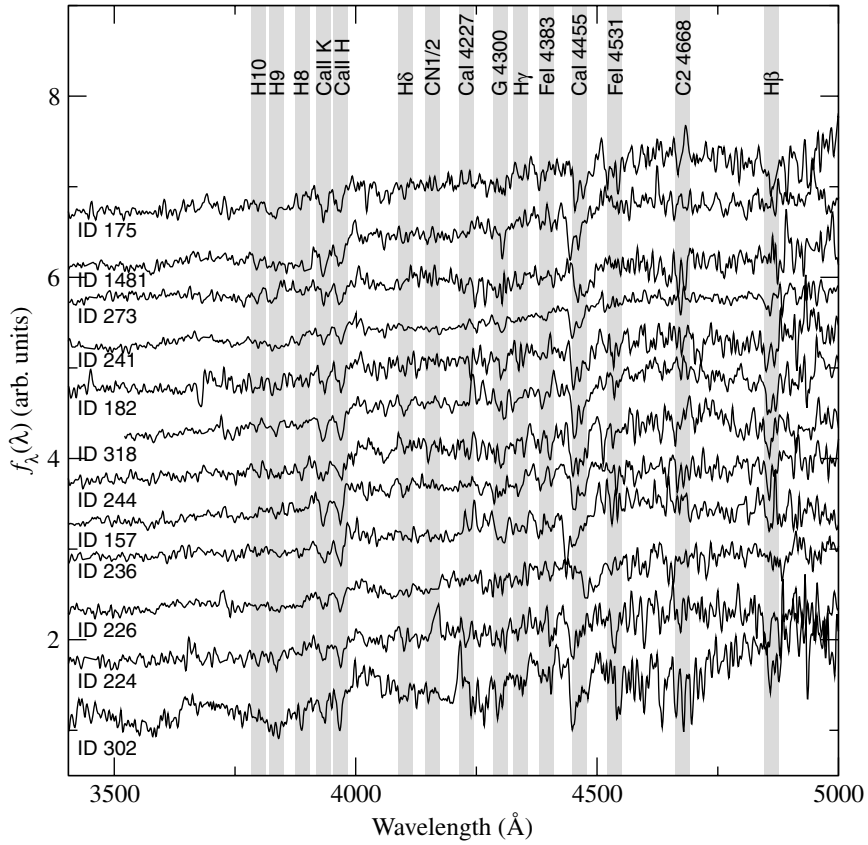

Figure 6. Spectra of the confirmed cluster members and prominent spectral features.

Table 2. Measured Lick indices, absolute magnitudes, luminous masses and synthesis results for each object. Column 1: galaxy identification; column 2: absolute i' magnitude; columns 3–12: Lick indices measured following the definitions given in Table 3; column 13: [O II]λ3727 EWs; column 14–17: percentual of flux contribution at 4200 Å of each template to the synthesis; column 18: luminous mass of the galaxy in units of 10^{11} $M_{\odot}$; column 19: projected distance (in kpc) to the estimated cluster centre. (*) [O II]λ3727 coincides with telluric line, not observable.

ID	$M_{AB,i'}$	Hδ_a	CN$_1$	CN$_2$	Ca I	G	Hγ_a	Fe I	C_2	Hβ	D_n	[O II]	per cent flux / per cent mass				$\frac{M_{LUM}}{M_{\odot}}$	R_P
													7.0 Gy	3.0 Gy	1.0 Gy	0.1 Gy		
(1)	(2)	(3)	(4)	(5)	(6)	(7)	(8)	(9)	(10)	(11)	(12)	(13)	(14)	(15)	(16)	(17)	(18)	(19)
302	−23.27	3.01 ± 1.03	−0.06 ± 0.03	−0.08 ± 0.04	–	3.67 ± 1.10	−3.03 ± 1.04	6.96 ± 1.08	–	7.61 ± 0.50	1.76 ± 0.01	–(*)	42.6	1.6	49.2	6.6	3.9	825
													88.4	1.4	10.0	0.1		
226	−23.38	−0.03 ± 2.15	0.00 ± 0.06	0.03 ± 0.07	0.51 ± 0.93	0.09 ± 1.83	1.10 ± 1.49	–	10.24 ± 1.95	−0.23 ± 0.99	1.62 ± 0.01	−10.6 ± 1.4	67.6	0.0	24.3	8.1	5.3	403
													96.5	0.0	3.4	0.1		
318	−23.74	0.23 ± 1.19	0.03 ± 0.03	0.08 ± 0.04	–	2.16 ± 1.19	−0.14 ± 1.13	–	0.81 ± 1.56	8.27 ± 0.69	1.58 ± 0.01	–	0.0	75.0	25.0	0.0	4.0	631
													0.0	92.9	7.1	0.0		
224	−23.09	−1.89 ± 1.76	–	–	3.32 ± 0.73	7.27 ± 1.39	−6.12 ± 1.64	7.03 ± 1.39	4.46 ± 2.02	2.63 ± 1.15	1.44 ± 0.01	–	47.6	52.4	0.0	0.0	4.5	460
													90.3	9.7	0.0	0.0		
1481	−23.98	0.04 ± 1.27	0.10 ± 0.04	0.13 ± 0.04	1.29 ± 0.67	5.85 ± 1.08	−5.10 ± 1.21	–	9.30 ± 1.46	2.00 ± 0.65	1.95 ± 0.01	–	100.0	0.0	0.0	0.0	10.5	123
													100.0	0.0	0.0	0.0		
236	−23.31	−1.57 ± 1.32	0.16 ± 0.04	0.21 ± 0.04	–	6.53 ± 1.01	−1.88 ± 1.21	–	3.43 ± 1.66	–	1.50 ± 0.01	–	74.5	25.5	0.0	0.0	5.1	87
													87.2	12.8	0.0	0.0		
157	−23.36	−0.30 ± 1.32	− 0.01 ± 0.04	0.02 ± 0.04	1.05 ± 0.72	4.29 ± 1.31	−1.45 ± 1.33	–	4.92 ± 2.03	7.02 ± 0.70	1.66 ± 0.01	−4.0 ± 0.8	76.0	6.0	8.0	10.0	4.7	282
													95.6	3.3	1.0	0.1		
244	−23.57	–	0.04 ± 0.04	0.11 ± 0.04	2.75 ± 0.66	5.66 ± 1.38	−7.31 ± 1.56	–	–	5.66 ± 1.38	1.87 ± 0.01	–	100.0	0.0	0.0	0.0	7.2	72
													100.0	0.0	0.0	0.0		
175	−23.30	−3.17 ± 2.01	0.00 ± 0.05	0.02 ± 0.06	0.63 ± 0.93	4.81 ± 1.53	−7.09 ± 1.65	–	–	8.33 ± 0.89	1.53 ± 0.01	−6.3 ± 1.1	0.0	92.3	0.0	7.7	2.9	388
													0.0	99.8	0.0	0.2		
182	−23.71	−0.28 ± 1.64	−0.04 ± 0.04	−0.04 ± 0.05	–	5.88 ± 1.34	−4.30 ± 1.53	–	–	8.86 ± 0.78	1.50 ± 0.01	−6.3 ± 0.9	0.0	88.4	0.0	11.6	4.1	709
													0.0	99.7	0.0	0.3		
273	−22.93	−1.75 ± 1.59	−0.15 ± 0.04	−0.23 ± 0.06	−0.09 ± 1.17	3.65 ± 1.82	−3.29 ± 1.77	–	6.03 ± 2.41	0.95 ± 0.90	1.22 ± 0.01	–	65.0	10.0	0.0	25.0	3.6	590
													93.4	6.2	0.0	0.4		
241	−24.27	−2.20 ± 1.40	0.15 ± 0.04	0.19 ± 0.05	–	3.31 ± 1.20	−0.26 ± 1.17	–	4.30 ± 1.67	2.41 ± 0.79	1.46 ± 0.01	–(*)	15.4	84.6	0.0	0.0	8.3	100
													29.8	70.2	0.0	0.0		

Table 3. Definitions of the Lick system (Worthey & Ottaviani 1997; Trager et al. 1998). Columns 3 and 4 give the pseudo-continua regions. (*) – indices in magnitudes.

Index	Line/band	$\Delta\lambda(PC_I)$	$\Delta\lambda(PC_S)$
$H\delta_a$	4083.500–4122.250	4041.600–4079.750	4128.500–4161.000
CN_1*	4142.125–4177.125	4080.125–4117.625	4244.125–4284.125
CN_2*	4142.125–4177.125	4083.875–4096.375	4244.125–4284.125
Ca II λ4227	4222.250–4234.750	4211.000–4219.750	4241.000–4251.000
G λ4300	4281.375–4316.375	4266.375–4282.625	4318.875–4335.125
$H\gamma_a$	4319.750–4363.500	4283.500–4319.750	4367.250–4419.750
Fe II λ4531	4514.250–4559.250	4504.250–4514.250	4560.500–4579.250
C_2λ4668	4634.000–4720.250	4611.500–4630.250	4742.750–4756.500
$H\beta$	4847.875–4876.625	4827.875–4847.875	4876.625–4891.625
	Δ_{inf}	Δ_{sup}	
$D_n(4000)$	3850.000–3950.000	4000.000–4100.000	

where I_i are the spectral indices, P_i the pseudo-continua and K_i are normalizing factors (necessary for the compatibility between indices with different typical values). For the Lick indices, K_i are the absolute differences between the maximum and minimum values possible for each index in the template spectra, and for $D_n(4000)$ it is the observed value for this index. For each observed spectrum we run the synthesis varying the w_i values with a step of 1 per cent, in two distinct runs: the first only with the solar-metallicity templates, and the next with only the subsolar-metallicity templates. Fig. 7 shows the observed spectra and the best-fitting synthetic result. Table 2 (columns 14–17) presents the synthesis result as the percentual contribution of each template to the total spectrum at 4200 Å, as well as the percentual mass contribution M(per cent) of each template.

It is very interesting that all the 12 galaxies of our sample are best fitted by the set of four solar metallicity rather than models with subsolar metallicity: the solutions with solar metallicity are better than the subsolar solutions by 2–80 per cent in χ (1–34 per cent in average differences between observed and synthetic parameters). The average dispersion of the observed quantities [EWs, continuum fluxes and the $D_n(4000)$ index] in relation to the synthetic ones in the best-fitting solution is about 5 per cent. Our results show that the bulk of the stars in the cluster galaxies are evolved ($t \geqslant 3$ Gyr). Three galaxies of the sample present significant (>20 per cent) flux contribution of stars with an age of 1.0 Gyr. In six objects we detected a contribution of very young ($t \sim 0.1$ Gyr) stellar populations, possibly associated with active star formation. The average percentual mass contribution of each template is 65.1, 33.7, 1.1 and 0.1 per cent for $t = 7.0$, 3.0, 1.0 and 0.1 Gyr, respectively.

In order to analyse the radial behaviour of the stellar population properties of the cluster, we have defined a parameter Q which unifies the age information and quantifies the amount of 'old' and 'new' stars present in each galaxy. We have defined it as

$$Q = \sum_{i=1}^{4} \frac{M \text{ (per cent)}}{100 \times t_i^2}, \tag{6}$$

where t_i is the age of the template i in Gyr. For an 'old' galaxy with 100 per cent of 7.0 Gyr stellar population, $Q \approx 0$, and for a 'young' galaxy with 100 per cent of stars with 0.1 Gyr, $Q = 100$. Fig. 8 shows the radial dependence of the Q parameter; the galaxies are plotted as circles whose radius is related to the galaxy luminous mass (see Section 6). It is evident from this figure that the galaxies whose stellar population appears to be old and single are in the central region of the cluster, while in the peripheric regions are the objects whose star formation was prolonged.

5.3 [O II] emission equivalent widths

The [O II]λ3727 was the only emission line detected in the spectra of four of our galaxies (for objects ID302 and ID241 this line was not detectable due to contamination of a telluric line). The other galaxies do not show any detectable emission line. The emission-line strengths in galaxies are associated with star formation regions, where young stars provide ultraviolet photons to ionize the gas. In addition, the EW of [O II] line can be used as indicator of the star formation rate. The EW of [O II]λ3727 for the observed galaxies was measured using the IRAF/NOAO packages, by fitting a Gaussian to this line; the line limits were estimated visually. The results are listed in Table 2.

Magris, Binette & Bruzual (2003) have computed an extensive set of stellar population synthesis models which contains the EWs and the intensities of the lines [O II]λ3727, $H\beta$, [O III]λ5007, $H\alpha$ and [N II]λ6584 as a function of the burst age. They were calculated assuming metallicities from $Z = 0.004$–0.03, a Salpeter IMF, star formation rates both continuous and exponential, in this latter case with varying time-scales τ, and whose stars cover a mass range with a fixed lower mass $M_{low} = 0.09$ $M_\odot$ and upper masses 40 $M_\odot \leqslant M \leqslant 120$ $M_\odot$. We have compared our measured EW[O II] with those of Magris et al. (2003) with solar metallicity. For each galaxy, we have calculated the theoretical $EW[O\,II]_{model}$ value using the mass contribution $M(\text{per cent})_i$ of each template as given in Table 2, using the expression

$$EW[O\,II]_{model} = \frac{\sum_{i=1}^{4} F_{L,i}\, M \text{ (per cent)}_i}{\sum_{i=1}^{4} F_{L,i}\, M \text{ (per cent)}_i / EW[O\,II]_i}, \tag{7}$$

where $F_{L,i}$ is the theoretical line flux. Fig. 9 shows this comparison. We first note that the theoretical predictions vary strongly depending on the model parameters. Nevertheless, the observed values could be well matched with models with 60 $M_\odot < M_{up} < 120$ $M_\odot$ and with star formation time-scales $1.0 < \tau < 3.0$ Gyr. The EW of the galaxy ID226 fits well a model with $\tau = 3.0$ Gyr and $M_{up} = 60\,M_\odot$ and galaxy ID157 fits a model with $\tau = 1.0$ Gyr and $M_{up} = 120$ $M_\odot$, while for galaxies ID175 and ID182 the observed EWs are fitted by intermediate values of these variables. In their N-body simulations, Diaferio et al. (2001) have found that the gas of newly accreted galaxies no longer cools to form stars and thus their star formation rate drops in time-scales of $1.0 < \tau < 2.0$ Gyr, agreeing with our results.

6 ABSOLUTE MAGNITUDES AND LUMINOUS MASSES

Absolute $M_{AB,i'}$ magnitudes were calculated using the synthetic spectra. First, we have transformed the synthetic spectra to the redshift of its galaxy and calibrated them using the i'_{AB} magnitudes. Note that the GMOS filters are defined in the AB system such that

$$i'_{AB} = -2.5 \log_{10} f_\nu(\text{erg s}^{-1}\,\text{cm}^{-2}\,\text{Hz}^{-1}) - 48.60. \tag{8}$$

We have then transformed the spectra again to the rest-frame system, applied the $(1+z)^2$ correction for cosmological dimming, recalculated the i' magnitude of the source and added the distance modulus, calculated to the galaxy redshift. Absolute magnitudes are given in

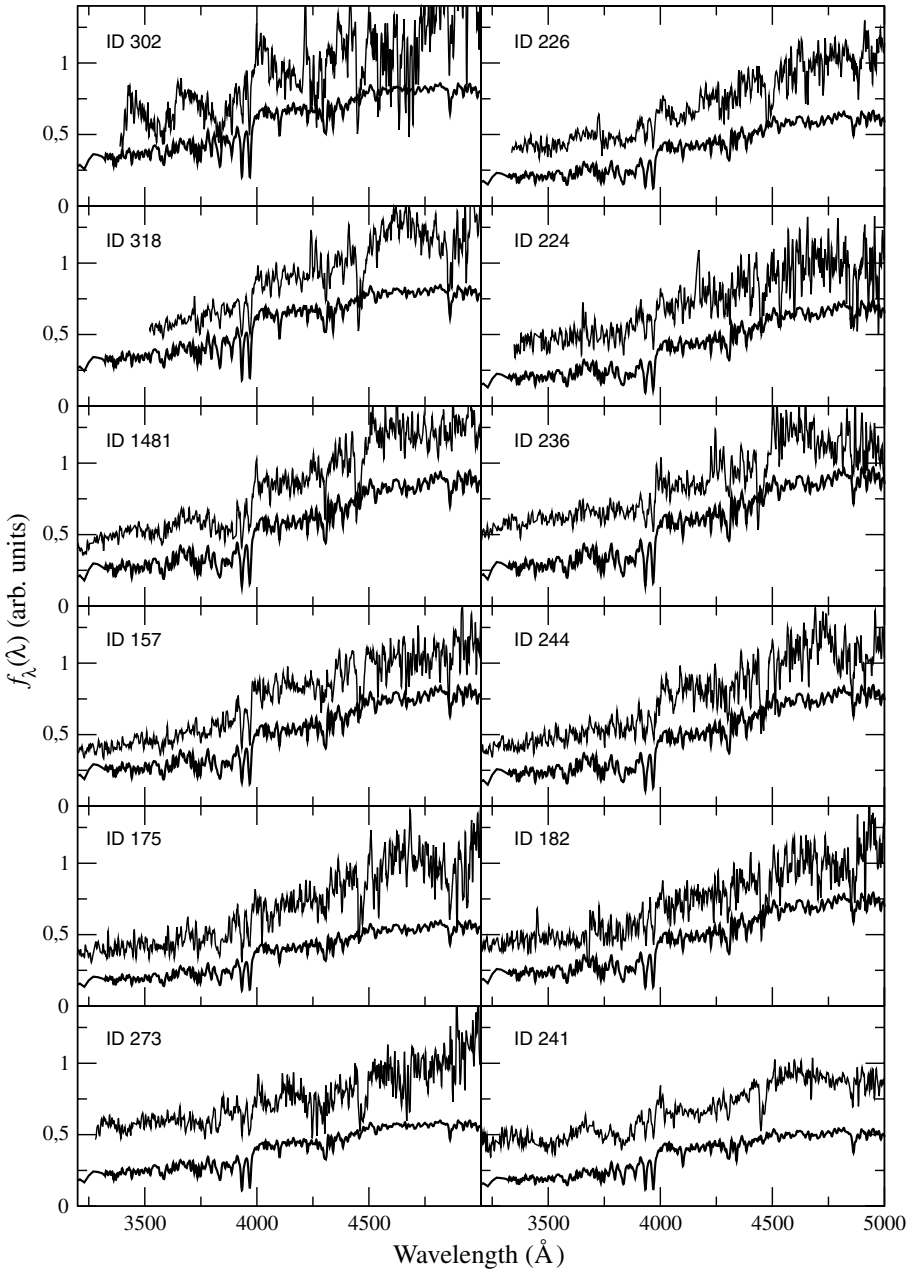

Figure 7. Synthesis results.

column 2 of Table 3. The 12 observed galaxies are very luminous; the range in luminosity is $-24.27 < M_{AB,i'} < -22.93$.

We have also estimated for these galaxies the luminous masses as follows. Each Bruzual & Charlot (2003) template is given in units of $L_\odot$ Å^{-1} and normalized to a total mass of 1 $M_\odot$. We can compare directly the flux density of these templates with the flux density of the calibrated synthetic spectrum given above, and therefore calculate both the total luminous mass associated with the calibrated spectrum and the mass fraction of each template in respect to the total mass, with the equation

$$M_{\rm LUM} = 4\pi \frac{f_\lambda(4200\text{Å})\,(3.0857 \times 10^{24} D_{\rm L})^2}{L_\odot \times L_{1\,M\odot}(4200\ \text{Å})}, \quad (9)$$

where $D_{\rm L}$ is the luminosity distance of the galaxy in Mpc (calculated from its redshift using the chosen cosmology), $f_\lambda(4200$ Å) is the calibrated flux of the galaxy (in erg s^{-1} cm^{-2} Å^{-1}) at 4200 Å and $L1\,M_\odot(4200$ Å) is the luminosity per solar mass of the synthesis solution. The total luminous mass for each galaxy is given in Table 2. We found that our galaxies span a moderate range in luminous mass (2.9×10^{11} $M_\odot < M < 10.5 \times 10^{11}$ $M_\odot$). The experimental uncertainty on the luminous mass is around 30 per cent; this value was estimated from the flux uncertainty at 4200 Å, since the $M_{\rm P}$ depends mainly on this value.

Besides the X-ray diffuse emission observed in clusters of galaxies (a tracer of the local gravitational potential), relic radio objects (and eventually diffuse radio emission) are often found in these systems. The existence of these radio sources in clusters of galaxies is usually explained considering that the source galaxy (for the radio relics) is in relative motion with respect to its circundant ICM. For LCDCS-S001, a source of radio emission at 1.4 GHz was detected

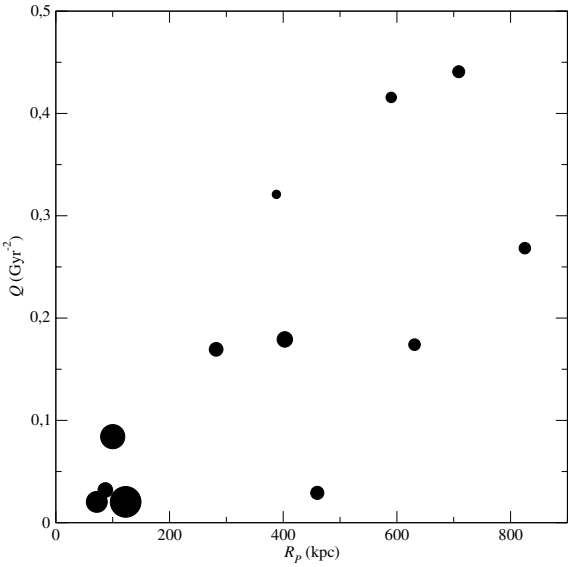

Figure 8. Radial dependence of the Q parameter; galaxies are plotted as circles, whose radius is related to the galaxy luminous mass.

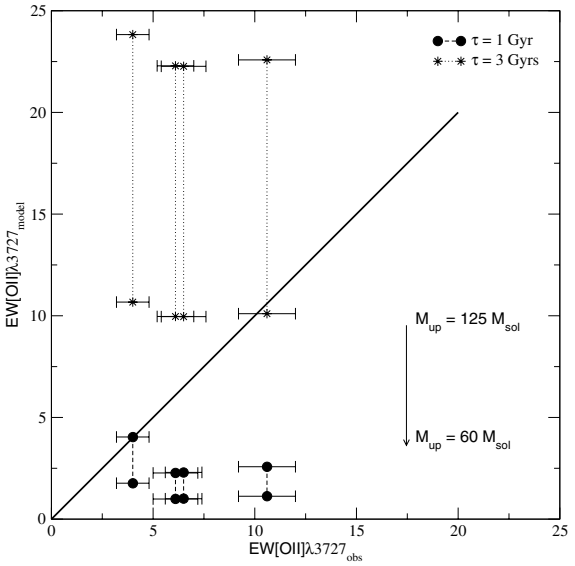

Figure 9. Comparison of the [O II]λ3727 EWs with the theoretical predictions of Magris et al. (2003). The thick line corresponds to a perfect match between model and observation; thin lines give an estimate of the uncertainties of the EW[O II] measurements.

with the VLA at the centre of this cluster (Becker, White & Helfand 1994), coinciding with the position of the most massive galaxies, as shown in Fig. 10. High-resolution radio imaging of this field would be valuable in order to identify the source object and to study its properties in detail.

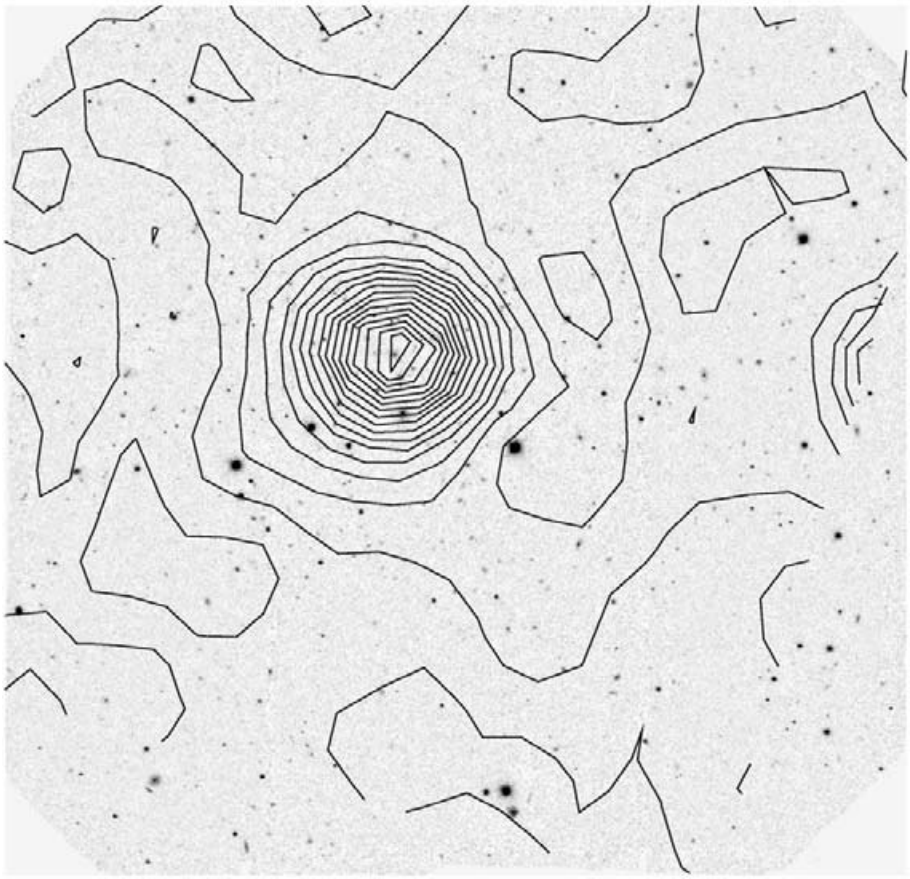

Figure 10. VLA 1.4 GHz contours overplotted on the field image. Note the remarkable coincidence between the visual centre of the cluster and the centre of radio emission.

7 CONCLUSIONS

We present kinematic parameters and stellar population properties of the galaxies members of the cluster LCDCS-S001, determined by spectroscopic data obtained with the GMOS instrument in the Gemini South Observatory. An i'-band image was obtained for the cluster field, where we have selected objects with non-stellar brightness profiles, providing a sample of objects of interest; multi-object spectroscopic observations centred on 7500 Å were obtained for 30 objects. Our most important results are summarized below.

(i) Spectral features were successfully identified for 20 objects, and were used to determine the galaxy redshift. The most common spectral features found for the galaxy cluster are the absorption lines Ca II H and Ca II K, the Balmer lines, G λ4300 and the emission line [O II]. We found that 12 objects are cluster members and estimate a median redshift of 0.709 for this cluster.

(ii) The velocity dispersion was calculated from the redshifts of the 12 cluster members, and was found to be $\sigma = 727 \pm 185$ km s^{-1}. The distribution of recession velocities of the cluster members was used to determine the projected mass of the cluster, and was found to be $3.54 \times 10^{14\ +2.33}_{\ -1.41}$ M$_\odot$.

(iii) Lick indices and the $D_n(4000)$ index were measured and used to determine the stellar population properties of the galaxies, by means of a spectral synthesis using the evolutive spectrophotometric models of Bruzual & Charlot (2003). We found that the stellar population of the cluster members can be well described by solar-metallicity templates, and that the bulk of stellar population of these galaxies is between 3.0 and 7.0 Gyr; in general, the flux contribution of younger stars in the spectra does not exceed 20 per cent at 4200 Å.

(iv) [O II]λ3727 emission was detected for four galaxies, three of which show the strongest contribution of younger stars among the galaxies observed. The EW of the [O II]λ3727 line was compared with H II regions models of Magris et al. (2003). We found that our EW[O II] values could be well matched with models with 60 M$_\odot$ < $M_{\rm up}$ < 120 M$_\odot$ and with star formation time-scales $1.0 < \tau < 3.0$ Gyr.

(v) The cluster centre is associated with radio (1.4 GHz) emission, what indicates that important dynamical effects are taking place in the core of this cluster. High-resolution radio imaging is necessary to identify the source properties.

ACKNOWLEDGMENTS

The authors acknowledge the financial support of the Brasilian Institution CNPq and also the referee Dave Carter for his useful comments.

REFERENCES

Barr J., Davies R., Jorgensen I., Bergmann M., Crampton D., 2005, AJ, 130, 445
Becker R. H., White R. L., Helfand D. J., 1994, in Crabtree D. R., Hanisch R. J., Barnes J., eds, ASP Conf. Ser., Vol. 61, Astronomical Data Analysis Software and Systems III. Astron. Soc. Pac., San Francisco, p. 165
Bruzual G., Charlot S., 2003, MNRAS, 344, 1000
Demarco R. et al., 2005, A&A, 432, 381
Diaferio A., Kauffmann G., Balogh M. L., White S. D. M., Schade D., Ellingson E., 2001, MNRAS, 323, 999
Gonzalez A. H., Zaritsky D., Dalcanton J. J., Nelson A., 2001, ApJS, 137, 117
Heisler J., Tremaine S., Bahcall J. N., 1985, ApJ, 298, 8
Henry J. P., 2002, in Chen L. W., Ma C. P., Ng K. W., Pen U. L., ASP Conf. Ser. Vol. 257, AMiBA 2001: High-z Clusters, Missing Barions, and CMB Polarization. Astron. Soc. Pac., San Francisco, p. 151
Jorgensen I., Bergmann M., Davies R., Barr J., Takamiya M., Crampton D., 2005, AJ, 129, 1249
Longhetti M., Rampazzo R., Bressan A., Chiosi C., 1998, A&AS, 130, 251
Magris G., Binette L., Bruzual G., 2003, ApJS, 149, 313
Maraston C., 2005, MNRAS, 362, 799
Postman M., Lubin L. M., Oke J. B., 1998, AJ, 116, 560
Salpeter E. E., 1955, ApJ, 121, 161
Small T. A., Ma C.-P., Sargent W. L. W., Hamilton D., 1998, ApJ, 492, 45
Trager S. C., Worthey G., Faber S. M., Burstein D., Gonzalez J. J., 1998, ApJS, 116, 1
van Dokkum P. G., Franx M., Fabricant D., Illingworth G. D., Kelson D. D., 2000, ApJ, 541, 95
Worthey G., Ottaviani D. L., 1997, ApJS, 111, 377

This paper has been typeset from a TEX/LATEX file prepared by the author.